The Astrophysical Journal, 910:21 (12pp), 2021 March 20 https://doi.org/10.3847/1538-4357/abdfd0

A Broadband View on Microquasar MAXI J1820+070 during the 2018 Outburst

J. Rodi[1], A. Tramacere[2], F. Onori[1,3], G. Bruni[1], C. Sànchez-Fernàndez[4], M. Fiocchi[1], L. Natalucci[1], and P. Ubertini[1]
[1] INAF—Istituto di Astrofisica e Planetologia Spaziali, via Fosso del Cavaliere 100, I-00133 Roma, Italy; james.rodi@inaf.it
[2] Department of Astronomy, University of Geneva, Ch. d'Ecogia 16, 1290, Versoix, Switzerland
[3] INAF—Osservatorio Astronomico d'Abruzzo, via M. Maggini snc, I-64100 Teramo, Italy
[4] European Space Astronomy Centre (ESA/ESAC), Science Operations Department, E-28691 Villanueva dela Canada, Madrid, Spain
Received 2020 July 30; revised 2021 January 21; accepted 2021 January 24; published 2021 March 23

Abstract

The microquasar MAXI J1820+070 went into outburst from 2018 mid-March until mid-July, with several faint rebrightenings afterward. With a peak flux of approximately 4 Crab in the 20–50 keV energy range, the source was monitored across the electromagnetic spectrum with detections from radio to hard X-ray frequencies. Using these multiwavelength observations, we analyzed quasi-simultaneous observations from April 12, near the peak of the outburst (∼March 23). Analysis of the X-ray spectrum found it indicative of an accreting black hole binary in the hard state, consistent with the flat/inverted radio spectrum and the accretion disk winds seen at optical wavelengths. Then, we constructed a spectral energy distribution spanning ∼12 orders of magnitude using modeling in `JetSeT`. The model is composed of an irradiated disk with a Compton hump and a leptonic jet with an acceleration region and a synchrotron-dominated cooling region. `JetSeT` finds that the spectrum is dominated by jet emission up to approximately 10^{14} Hz, after which disk and coronal emission dominates. The acceleration region has a magnetic field of $B \sim 1.6 \times 10^4$ G, a cross section of $R \sim 2.8 \times 10^9$ cm, and a flat radio spectral shape naturally obtained from the synchroton cooling of the accelerated electrons. The jet luminosity is $>8 \times 10^{37}$ erg s^{-1} ($>0.15 L_{\rm Edd}$), compared to an accretion luminosity of $\sim 6 \times 10^{37}$ erg s^{-1}, assuming a distance of 3 kpc. Because these two values are comparable, it is possible that the jet is powered predominately via accretion with only a small contribution needed from the Blanford–Znajek mechanism from the reportedly slowly spinning black hole.

Unified Astronomy Thesaurus concepts: X-ray transient sources (1852); Stellar mass black holes (1611); Spectral energy distribution (2129)

1. Introduction

The term "microquasar" was first applied to the persistent black hole candidate 1E 1740.7–2942 after detecting radio jets from the known hard X-ray source (Mirabel et al. 1992) that were similar to radio-loud active galactic nuclei (AGNs). Jets were later found to be common features in accreting BH systems in the hard state. Multiwavelength studies showed correlations between radio and X-ray luminosities (Gallo et al. 2003), indicating a relationship between the emission mechanisms despite a large physical separation between the two. Additionally, this correlation holds also for supermassive BHs in AGNs when accounting for mass (Merloni et al. 2003), thus linking the mechanisms in stellar mass and supermassive BHs. Therefore, understanding the jet and X-ray components in microquasars can shed light on AGNs.

The low-mass X-ray binary MAXI J1820+070 (=ASASSN-18ey) was first detected on 2018 March 6.59[5] with the All-Sky Automated Survey for SuperNovae (Shappee et al. 2014) and was detected ∼6 days later by the MAXI/GSC at 2018 March 11 19:48 UTC (Kawamuro et al. 2018). With a peak flux of ∼4 Crab in the 20–50 keV energy band (Roques & Jourdain 2019) and a long decay, the source was a good candidate for numerous observing campaigns across the electromagnetic (EM) spectrum (e.g., Tucker et al. 2018; Muñoz-Darias et al. 2019; Bright et al. 2020; Stiele & Kong 2020) to explore various aspects of the source. Combining observations from various campaigns enables studying the various emission processes together.

Therefore, we compiled quasi-simultaneous observations from public archives, Astronomer's Telegrams, and Gamma-ray Coordination Network Circulars to construct the widest possible frequency range, and we were able to find detections covering nearly 12 orders of magnitude from the meter-wavelength frequencies to hard X-rays on 2018 April 12 (MJD 58220). With this spectral energy distribution (SED), we studied the spectral components independently before investigating them jointly by constructing a model consisting of a leptonic jet, an irradiated disk, and a corona, using the `JetSeT` software.[6]

2. Observations

Figure 1 shows the initial period of MAXI J1820+070 outburst in several wavelengths across the spectrum using data from Swift/BAT (black diamonds), Swift/XRT (green squares; Stiele & Kong 2020), and 4.7 GHz RATAN (blue triangles; Trushkin et al. 2018). The XRT and RATAN data have been normalized to be on the same scale as the BAT data. The period of the observations used in this work is bracketed in red.

In the following, we give information about the different simultaneous observations collected from archives, covering different bands from radio to gamma ray on 2018 April 12. Further details can be found in Table 1.

2.1. JVLA

We retrieved calibrated Karl G. Jansky Very Large Array (VLA) data for experiment VLA/18A-470 from the National Radio Astronomy (NRAO) online archive. The JVLA antennas, in A configuration, were split into three subarrays in order to obtain simultaneous observations at six different central frequencies

[5] http://www.astronomy.ohio-state.edu/asassn/transients.html
[6] https://jetset.readthedocs.io/en/latest/

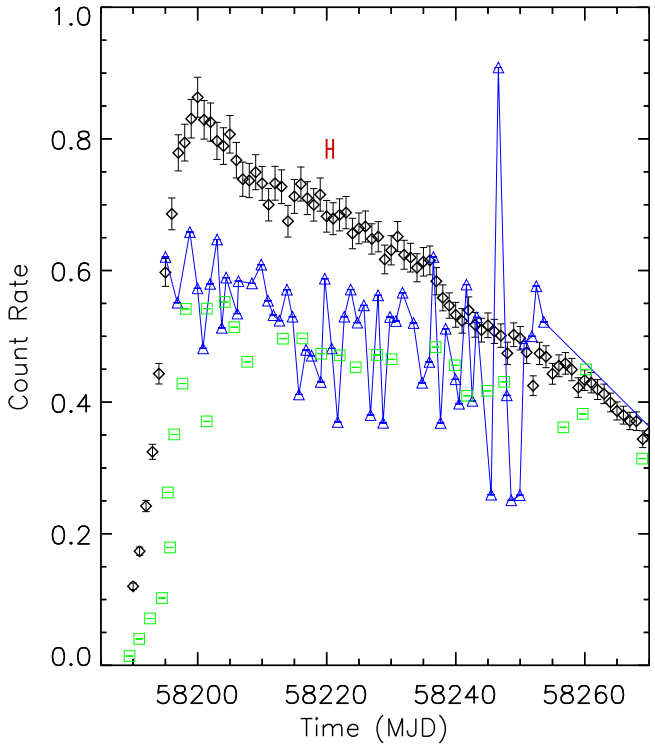

Figure 1. Top: light curves for Swift/BAT 15–50 keV (black diamonds), 0.3–10 keV Swift/XRT (green squares), and 4.7 GHz RATAN (blue triangles) for the initial phase of the outburst. The time span of observations analyzed in this work is denoted in red.

Table 1
MAXI J1820+070 Observations Log

Instrument	Start Time (UTC)	Stop Time (UTC)
VLITE	07:25:00 12-04-2018	13:07:00 12-04-2018
JVLA	07:15:00 12-04-2018	13:14:50 12-04-2018
ALMA	08:13:18 12-04-2018	09:20:16 12-04-2018
X-shooter	07:41:08 12-04-2018	08:15:48 12-04-2018
EPIC-pn	07:27:58 12-04-2018	09:39:28 12-04-2018
OMC	23:41:01 11-04-2018	14:00:21 12-04-2018
ISGRI	23:41:01 11-04-2018	14:00:21 12-04-2018

(4.7, 7.5, 8.5, 11, 20.7, and 25.5 GHz). Data were imaged using `CASA` (`Common Astronomy Software Applications` package) version 5.6.2[7] following standard procedures.

2.2. ALMA

Atacama Large Millimeter/submillimeter Array (ALMA) data for project 2017.1.01103.T were retrieved from the ESO archive and pipelined at the Italian node of the European ALMA Regional Centre (INAF-Istituto di Radioastronomia, Bologna). Imaging was performed with `CASA` version 5.1.1, separately for each one of the four spectral windows (spw) present in the data (Band 7, spw 5, 7, 9, and 11), corresponding to the following central frequencies: 336, 338, 348, and 350 GHz (Bonato et al. 2018).

2.3. VLT/X-shooter

A number of observations of MAXI J1820+070 were performed with the X-shooter spectrograph (Vernet et al. 2011) in the framework of the ESO program 0101.D-0356(A). We retrieved the processed spectra obtained during the 2018 outburst on April 12 from the European Southern Observatory (ESO) archive science portal. These data have been reduced by using the ESO X-shooter pipeline V2.7.0 and cover the 3000–25000 Å wavelength range. The observations were conducted in nodding configuration with the slit oriented at the parallactic angle and using slit widths of $1\farcs3 \times 11$, $1\farcs2 \times 11$, and $1\farcs2 \times 11$ for the UVB, VIS, and near-IR (NIR) arm, respectively. This configuration yields a spectral resolution $R = \lambda/\Delta\lambda$ of 4100, 6500, and 4300 for the UVB, VIS, and NIR arm, respectively. The observing conditions were good, with a seeing of $0\farcs47$ and an average air mass of the source during the acquisition of $1\farcs3$. The total exposure times are 1640, 1300, and 1520 s for the UVB, VIS, and NIR arm, respectively. The reduced spectra have been corrected for the foreground extinction using the Cardelli function (Cardelli et al. 1989), with $R(V) = 3.1$ and $A_V = 0.627$ mag (Schlafly & Finkbeiner 2011, via the NASA/IPAC Extragalactic Database (NED)).

In order to estimate the slit-loss effect in the X-shooter spectra, we first applied standard aperture photometry on the i' acquisition image using the `iraf` task `phot`. The zero-point was calibrated using the stars in the Panoramic Survey Telescope and Rapid Response System (Pan-STARRS1 Flewelling et al. 2020) catalog.

From the aperture photometry we obtain an i'-band apparent magnitude of $m_{AB} = (12.20 \pm 0.11)$ mag, corrected for foreground extinction. The derived flux at the filter central wavelength is $\lambda F_i = (2.01 \pm 0.2) \times 10^{-10}$ erg s^{-1} cm^{-2}, which is in agreement with the average flux measured from the spectrum in the 7300–7600 Å wavelength range: $\lambda F_i = (1.8 \pm 0.7) \times 10^{-10}$ erg s^{-1} cm^{-2}.

2.4. XMM-Newton/EPIC-pn

XMM-Newton ToO observations were carried out from 2018 April 12 07:27:58 to 09:39:28 UTC (obsid 0820880501) using burst mode. The European Photon Imaging Camera (EPIC)-pn data were analyzed using the standard procedures with the Science Analysis System (SAS) software version `xmmsas_20190531_1155-18.0.0`.[8]

2.5. INTEGRAL

The INTErnational Gamma-Ray Astrophysics Laboratory (INTEGRAL) observed MAXI J1820+070 every 2–3 days between March 16 and May 8, via a series of Target of Opportunity (ToO) observations. For this work, we selected the data covering the interval (UTC) from 2018 April 11 23:41:01 to 2018 April 12 11 14:00:21 (INTEGRAL revolution 1941). Here we focus on the analysis of data provided by the Integral Soft Gamma-Ray Imager (ISGRI; 18–1000 keV) placed on the upper layer of the detector plane of the Imager on Board the INTEGRAL Satellite (IBIS) telescope (Ubertini et al. 2003) and by the Optical Monitoring Camera (OMC; 500–600 nm) instruments. The data were analyzed using the Offline Science Analysis software (OSA) v11.0 available at the INTEGRAL Science Data Center (ISDC).[9] We followed standard analysis procedures.

[7] https://casa.nrao.edu

[8] https://www.cosmos.esa.int/web/xmm-newton/sas-threads

[9] https://www.isdc.unige.ch/integral/analysis

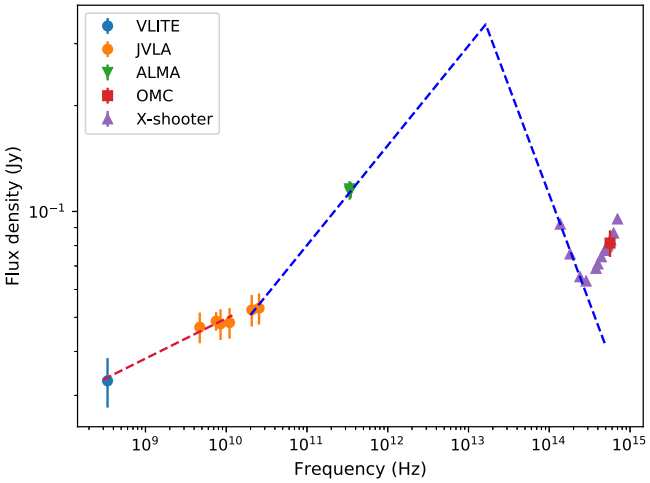

Figure 2. Jet emission between radio and optical bands, as reconstructed from VLITE, JVLA, ALMA, and X-shooter observations. The blue dashed line is a broken power law, used to identify the synchrotron peak frequency and flux density. The red line is a power-law fit of the most expanded region of the jet, considered as a physically separated component. The optical flux from OMC is also shown, although not considered for the fit.

3. Results and Discussion

3.1. The Compact Jet Emission

With the collected flux densities between radio and UV bands, we built the jet SED. In addition to the JVLA and ALMA data mentioned above, we considered data from the Very Large Array Low-band Ionosphere and Transient Experiment (VLITE; Clarke et al. 2016), also collected on 2018 April 12 (Polisensky et al. 2018). We show in Figure 2 data from JVLA, ALMA, X-shooter, and OMC. For X-shooter, we considered only the part of the spectrum not affected by absorption/emission features, and we averaged values for each of these intervals to obtain continuum flux density values. In this way, we calculated 12 photometric measurements (Table 2) covering the interval from NIR to UV. The overall shape of the X-shooter spectrum shows a break, resulting in a change of the spectral index, at about 2×10^{14} Hz. This is most probably the frequency at which the broadband SED is no longer dominated by the jet synchrotron emission, while the accretion disk thermal emission increases (see Section 4). The single value from OMC is in good agreement with the X-shooter photometry.

We fitted the radio to optical data set with a broken power law to identify the synchrotron peak frequency and the spectral slopes of the optically thin and thick regions (Russell et al. 2013). We used the Astropy `BrokenPowerLaw1D` function (see Astropy Collaboration et al. 2013; Price-Whelan et al. 2018) adopting the `LevMarLSQFitter` routine to perform a Levenberg–Marquardt least-squares statistic. We excluded from the fit the X-shooter points above the third one (Optical and UV ranges) since they show a turn-up of the flux density likely due to accretion disk emission. Similarly, we did not consider data points below 20 GHz, since they show a different slope, probably belonging to a physically distinct (and more expanded) radio jet component. We obtained a synchrotron peak frequency of $(1.6 \pm 0.2) \times 10^{13}$ Hz. The estimated slope for the optically thick part of the spectrum is $\alpha_{\rm thick} = 0.28 \pm 0.02$, and $\alpha_{\rm thin} = -0.61 \pm 0.01$ for the optically thin one (adopting the convention $S \propto \nu^{\alpha}$, where S is the flux density, ν the frequency, and α the spectral index). The slope of the lower-frequency radio SED (0.3−10 GHz), fitted with the `PowerLaw1D` Astropy function, is $\alpha = 0.11 \pm 0.02$. In Section 4, a detailed physical model of this source is presented and provides a more precise estimate of the jet parameters.

Table 2
Collected Flux Densities for the Jet Modeling

Instrument	Frequency (Hz)	Flux Density (Jy)
VLITE	3.39E+08	0.033 ± 5.3
JVLA	4.70E+09	0.0469 ± 0.0047
	7.50E+09	0.0488 ± 0.0029
	8.50E+09	0.0479 ± 0.0048
	1.10E+10	0.0483 ± 0.0048
	2.07E+10	0.0525 ± 0.0054
	2.55E+10	0.0530 ± 0.0054
ALMA	3.36E+11	0.116 ± 0.006
	3.38E+11	0.114 ± 0.006
	3.48E+11	0.115 ± 0.006
	3.50E+11	0.110 ± 0.006
X-shooter	1.37E+14	0.0920 ± 0.0002
	1.81E+14	0.0757 ± 0.0012
	2.40E+14	0.0652 ± 0.0003
	2.86E+14	0.0634 ± 0.0006
	3.79E+14	0.0689 ± 0.0007
	4.00E+14	0.0709 ± 0.0002
	4.42E+14	0.0743 ± 0.0003
	4.87E+14	0.0775 ± 0.0005
	5.15E+14	0.0794 ± 0.0002
	5.32E+14	0.0803 ± 0.0003
	5.76E+14	0.0831 ± 0.0005
	6.27E+14	0.0868 ± 0.0003
	7.00E+14	0.0952 ± 0.0004
OMC	5.66E+14	0.0813 ± 0.0071

3.2. Accretion Disk Winds

Muñoz-Darias et al. (2019) discovered accretion disk winds in MAXI J1820+070 during both the 2018 hard-state rise and decay. Absorption wind signatures were detected in the blue wings of He I λ5876 and λ6678 emission lines, reaching a maximum terminal velocity (v_t) of 1200 km s^{-1} in one of the epochs. For Hα, both a blue-wing broadened emission-line profile, implying a wind component of 1800 km s^{-1}, and a superimposed absorption trough with $v_t = 1200$ km s^{-1} were found. Those authors collected several epochs from 2018 March 15 to November 4, allowing them to follow the evolution of the winds from the hard state to the disappearance during soft state and back.

The VLT/X-shooter data presented in this work add an epoch to monitoring in Muñoz-Darias et al. (2019), falling in an uncovered time window of 1 month between March 26 and April 23. We normalized these spectra by dividing them for the continuum emission, fitted with a third-order spline3 function by using the IRAF task `continuum`. These spectra are rich with emission lines from the UVB to the NIR arms. Following the Muñoz-Darias et al. (2019) analysis, we explored the presence of wind signatures linked to the mentioned emission lines (He I and Hα) and found significant absorption on the left wing of He I λ5876. In Figure 3 (left panel) we show the relative portion of the spectrum, with the absorption features highlighted in purple. We consider as bona fide absorption troughs the ones with a dip of at least three times the continuum rms. A prominent He I absorption feature is visible between −700 and −900 km s^{-1}, showing the same profile as the correspondent emission line. This one has a v_t of 880 km s^{-1}. Further blueward absorption

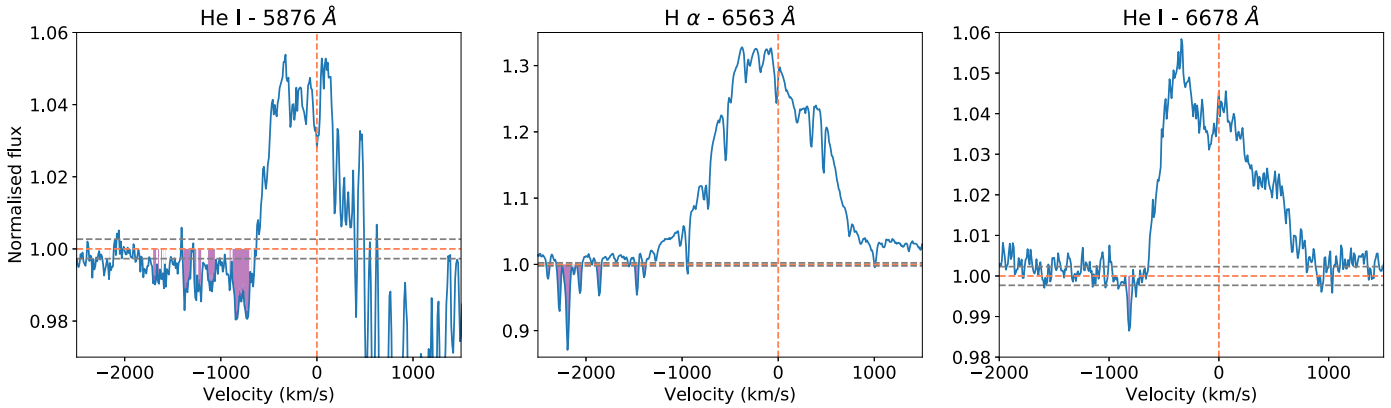

Figure 3. Accretion disk wind absorption features in the VLT/X-shooter optical spectrum. Normalized flux errors are shown as the cyan shaded area. Troughs deeper than 3 × rms are highlighted in purple. The rms value is 0.0027 for the He I λ5876 region, while it is 0.0023 for the Hα and He I λ6678 regions. The gray dashed lines indicate the 1 ± rms intervals.

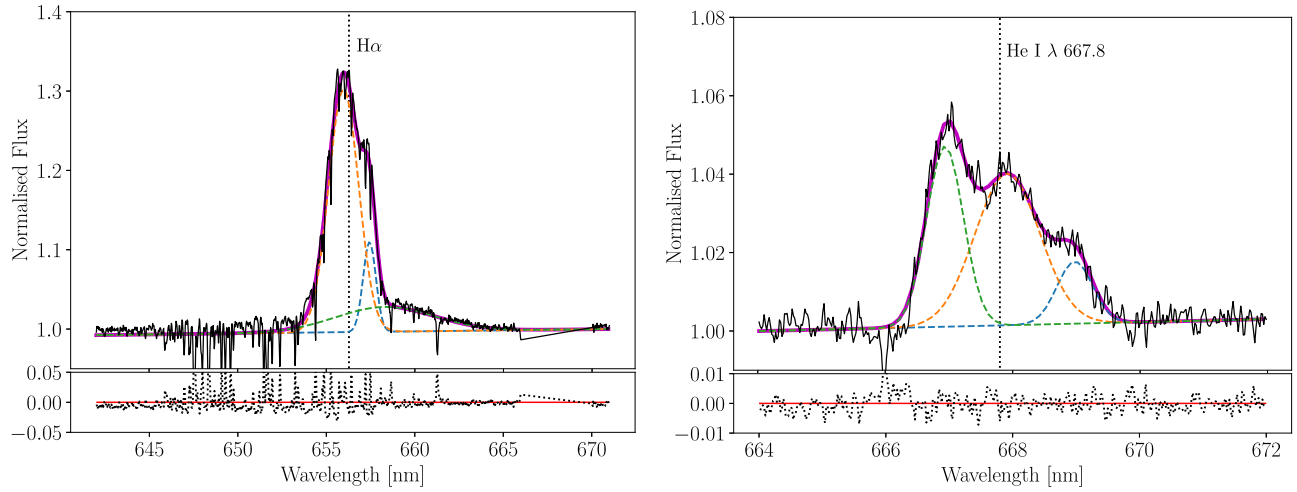

Figure 4. Fits of the emission-line profiles for Hα (left panel) and He I λ6678 (right panel). The residuals of the fits are shown at the bottom of each panel. The line profiles are modeled with Gaussian components (colored dashed lines). The total fitting model is represented by the magenta solid line.

features are visible, but since they are narrower and not connected to the previous ones, we consider those as not related to the accretion disk wind. The same is true for the narrow absorption features detected blueward of the Hα emission line (Figure 3, middle panel). For the He I λ6678 line, a single absorption trough is detected between −800 and −850 km s^{-1} (Figure 3, right panel) with a v_t of −825 km s^{-1}.

During this period, we observe strong asymmetries in the emission lines that are commonly observed in lines emitted from the disk, particularly in the He I λ6678 and in the Hα. Therefore, we explored line profile properties by applying multicomponent Gaussian fits using the `python` packages `curvefit` and `leastsq`. In Figure 4 we show the result of this analysis for Hα (left panel) and He I λ6678 (right panel). The Hα line analysis has been performed in the wavelength region 644 −670 nm, which includes the feature of interest and the local continuum. In this case we have ignored from the fit the He I emission line, which falls at the end of the analyzed wavelength range. The Hα profile is well modeled by two narrow Gaussian components, and only one broad Gaussian component is needed to fit the red wing of the emission line. We note the absence of a blueshifted broad wing, which has been observed in Muñoz-Darias et al. (2019), as well as P Cygni profile signatures. However, a forest of narrow absorption lines is clearly visible in the blue region of the Hα. The two narrow components are characterized by a central wavelength (λ_c) and an FWHM of $\lambda_c = 6574.4 \pm 0.4$ Å, FWHM $= 389 \pm 20$ km s^{-1} and $\lambda_c = 6559.8 \pm 0.3$ Å, FWHM $= 914 \pm 18$ km s^{-1}, respectively, while the broad red wing is centered at $\lambda_c = 6583.0 \pm 3.0$ Å and has FWHM $= 2982 \pm 210$ km s^{-1}. From the redshift of the broad wing with respect to the Hα rest-frame wavelength we derive an outflow velocity of $v = 923 \pm 14$ km s^{-1}, while the separation between the two narrow components is ∼667 km s^{-1}.

For the He I λ6678 line analysis we used the wavelength region 664–672 nm, which includes also the local continuum but excludes the wavelength range in which the Hα falls. The He I λ6678 line profile is well modeled by three Gaussian components. The first one is well centered on the rest-frame He I wavelength with a $\lambda_c = 6679.2 \pm 0.4$ Å and has FWHM $= 536 \pm 54$ km s^{-1}. The two remaining Gaussians are blueshifted and redshifted by ∼450 km s^{-1} with respect to the first component and are characterized by $\lambda_c = 6669.4 \pm 0.2$ Å, FWHM $= 307 \pm 12$ km s^{-1} and $\lambda_c = 6689.7 \pm 0.3$ Å, FWHM $= 295 \pm 29$ km s^{-1}, respectively.

As a whole, the detected optical disk wind features show properties in between what was found in the hard- and soft-state epochs collected by Muñoz-Darias et al. (2019), confirming the decreasing trend of the optical wind between the two states of the source.

3.3. Soft X-Ray

We fitted the XMM-Newton/EPIC-pn spectrum in the 0.5–12 keV energy range in XSPEC using a Tbabs*Powerlaw model. With this model we derive the following parameters: $nH = (0.13 \pm 0.04) \times 10^{22}$ cm^{-2}, $kT_{\rm bb} = 0.24 \pm 0.03$ keV, and $\Gamma = 1.65 \pm 0.08$ with $\chi 2/\nu = 1.00$.

3.4. Hard X-Ray

We fitted the INTEGRAL/IBIS/ISGRI spectrum in the 30–400 keV energy range. A systematic 1.5% error was added to the data, following OSA 11 standard recommendations.[10] A power-law fit to the data in XSPEC found a photon index of $\Gamma = 2.41 \pm 0.01$ and a $\chi^2/\nu = 71.80$. The spectrum deviates from a simple power-law model, especially at high energies, with residuals suggesting a Comptonized spectrum. Fitting the data with a CompTT model using a photon temperature of 0.24 keV fixed to the $kT_{\rm bb}$ value from XMM finds a better fit, with $k_T = 36.4 \pm 0.9$ keV, $\tau = 1.27 \pm 0.05$, and $\chi^2/\nu = 6.21$. When including a reflecting component (REFLECT) with the reflection fraction fixed to 1, the fit improves to $\chi^2/\nu = 3.45$ with $k_T = 38 \pm 1$ keV and $\tau = 1.44 \pm 0.06$. Following Roques & Jourdain (2019), a cutoff power law was added, Reflect*(CompTT)+cutoff, with $\Gamma = 1.6$ and a cutoff energy of 200 keV that improved the fit to 0.71 and has fit parameters $k_T = 27 \pm 4$ keV, $\tau = 2.2$.

To characterize the X-ray spectrum, a joint fit was performed between the two instruments spanning 0.5–400 keV using the model Tbabs*Reflect*(diskbb+CompTT)+Tbabs*cutoff and found best-fit parameters of $kt_{\rm BB} = 0.27 \pm 0.01$ keV, $kT = 27 \pm 1$ keV, and $\tau = 2.2 \pm 0.1$ with $\chi^2/\nu = 0.95$.

Using this joint spectrum, we calculated the accretion luminosity in the 1–200 keV energy range and found a value of $\sim 6 \times 10^{37}$ erg s^{-1} for a distance 3 kpc.

3.4.1. IR—Hard X-Ray Spectrum

Subsequently, we fit our data from the NIR to hard X-rays using an irradiated disk model to compare with Shidatsu et al. (2018), which analyzed a similar energy range using observations from March 24. The irradiated disk model accounts for the effects of the Comptonized emission on the accretion disk and the soft-excess that is seen in the hard state (Gierliński et al. 2009). Figure 5 shows the spectrum from 0.001 to 400 keV, with the diskir model shown as a solid red line and the power-law component of the diskir+po model shown as a dashed black line. The power law is used to model the high-energy cutoff power-law component in the previous section. Table 3 contains the fit parameters using a diskir model with and without an additional power-law component. We found that including a power-law component improved the fit at high energies and reduced the χ^2/ν from 1.30 to $\chi^2/\nu = 0.97$ with an F-test probability of 3.7×10^{-8}.

The origin of the power-law component is unclear. As shown in the SED modeling in Section 4.3.3, the expected jet flux is too low for the component to be jet emission at those energies. However, the emission could possibly be from Comptonization of nonthermal electrons as in the case of GRS 1716–249 (Bassi et al. 2020).

[10] https://www.isdc.unige.ch/integral/analysis

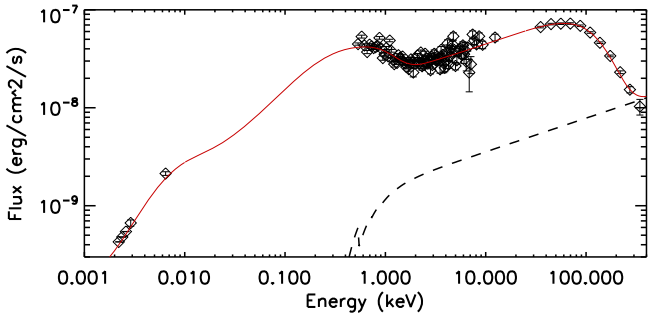

Figure 5. MAXI J1820+070 spectrum from 0.001 to 400 keV. The diskir model is shown with a solid red line, and the po component is shown with a black dashed line.

Table 3
Irradiated Disk Fit Parameters

	diskir	diskir+po
$kT_{\rm disk}$(keV)	0.116 ± 0.007	0.122 ± 0.007
Γ	1.78 ± 0.02	1.70 ± 0.04
kT_e (keV)	58 ± 4	37 ± 4
L_C/L_D	4.7 ± 0.5	4.7 ± 0.6
$f_{\rm out}$	$(1 \pm 40) \times 10^{-7}$	$(4 \pm 15) \times 10^{-2}$
$\log(r_{\rm out})$	3.45 ± 0.04	3 ± 1
$\Gamma_{\rm po}$	...	1.6 ± 0.3
Norm$_{\rm po}$	...	1.0 ± 1.7
χ^2/ν	1.30	0.97

4. Broadband SED Modeling

We modeled the broadband SED of MAXI J1820+070 using a combination of jet leptonic models and irradiated disk and corona models implemented in the Jets SED modeler and fitting Tool (JetSeT;[11] Tramacere 2020; Tramacere et al. 2011, 2009). A more accurate description of the model is discussed in A. Tramacere (2021, in preparation). We assume that the optical/UV up to keV energies is dominated by disk irradiation and coronal emission. The emission in the millimeter to optical region is dominated by the nonthermal emission of leptons accelerated in the jet by shock and/or stochastic acceleration, and we assume that the break at $\approx 1.5 \times 10^{13}$ Hz is due to the transition from the optically thin to the optically thick synchrotron emission. The radio emission is dominated by the terminal part of the jet that starts beyond the acceleration region and extends up to a distance of $\approx 1 \times 10^{15}$ cm according to Bright et al. (2020). A schematic view of the model is provided in Figure 6.

4.1. Individual Model Component Description

In the following we describe the implementation of each model component.

4.1.1. Irradiated Disk and Hot Corona

To model the UV to hard X-ray emission, we have used the disk Comptonization plus disk irradiation model, DiskIrrComp implemented in JetSeT. The DiskIrrComp is based on the diskir model (Gierliński et al. 2009) and the Comptonization model of Zdziarski et al. (2009). In detail, we assume a classical multitemperature disk with an inner

[11] https://jetset.readthedocs.io/en/latest/

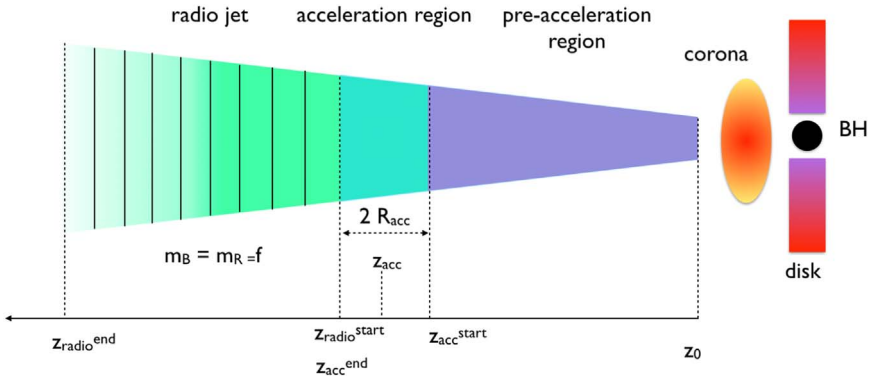

Figure 6. Schematic view of the jet model setup. The purple region identifies the preacceleration region, the cyan region identifies the acceleration region, and the green region identifies the radio jet. The z-axis on the bottom shows the starting and end point of each region. The acceleration region is assumed to be spherical with a radius equal to the jet cross section. The vertical black lines in the radio jet region mark qualitatively the division of region in slices.

temperature $T_{\rm Disk}$ and an extension $R_{\rm in} = 3R_S$ to $R_{\rm out}$, expressed by the dimensionless parameters $r_{\rm in} = R/R_{\rm in}$ and $r_{\rm out} = R/R_{\rm out}$. The disk spectrum is modified owing to the reprocessing of irradiated emission from the disk itself and from the corona Compotonization tail. The corona emission is described by a power law with an exponential cutoff with a photon index $\Gamma_{\rm Comp}$ and a cutoff energy $E_{\rm Comp} = kT_e$ where kT_e is the corresponding electron temperature. The Compton hump component is described by a power law with exponential cutoff with a photon index $\Gamma_{\rm hump}$ and a cutoff energy $E_{\rm hump}$. We refer to this model as `Comp. hump`. The normalization of the Compton tail component is parameterized as a fraction of the disk luminosity $L_{\rm Disk}$ according to $L_{\rm Comp}^{\rm ratio} = L_C/L_{\rm Disk}$. The total bolometric flux will be $L_{\rm bol} = L_{\rm Disk} + L_{\rm rep} + L_C$, where $L_{\rm rep}$ represents the thermalized fraction $f_{\rm in}$ of L_C thermalized within $r_{\rm in}$ and $r_{\rm irr} = R_{\rm irr}/R_{\rm in}$, where $R_{\rm irr}$ is the radius of the inner disk irradiated by the Compton tail. A fraction $f_{\rm out}$ of the bolometric luminosity will irradiate the outer disk. The irradiation creates a shoulder with a spectral trend $f_{\rm out} \propto L_{\rm bol}\nu^{-1}$ that extends between $\nu_1 = 3kT(r_{\rm out})$ and $\nu_2 = 3kT(r_t)$, where r_t is the transitional radius between gravitational and irradiation energy release. This effect depends strongly on $r_{\rm out}$ and $f_{\rm out}$, and it is present even without corona Comptonization, because it represents the disk self-irradiation. The presence of a Comptonization component will provide a further heating of the disk in the inner part modifying the pure gravitational temperature profile.

4.1.2. Preacceleration and Acceleration Region

We assume that electrons in the preacceleration region close to the base of the jet are described by a thermal plasma with cooling dominated by adiabatic losses. Once the particles approach the acceleration region, they are accelerated under the effect of diffusive shock acceleration and/or stochastic acceleration and the corresponding energy distribution can be modeled by a power law with a high-energy cutoff

$$N_{e,\rm acc}(\gamma) = N\gamma^{-s}\exp(-\gamma/\gamma_{\rm cut}), \quad (1)$$

where the value of $\gamma_{\rm cut}$ takes into account the balance between cooling and acceleration terms. The index s is dictated by the competition of the acceleration timescales and escape timescales (Tramacere et al. 2011). We assume that the acceleration region extends from $z_{\rm acc}^{\rm start}$ to $z_{\rm acc}^{\rm end}$, with cross section $R_{\rm acc}$ equal to the average cross section of the jet at $z = (z_{\rm acc}^{\rm start} + z_{\rm acc}^{\rm end})/2$, with $z_{\rm acc}^{\rm end} - z_{\rm acc}^{\rm start} = 2R_{\rm acc}$. The emission from the acceleration region is reproduced using the jet leptonic model `Jet` implemented in `JetSeT`, and we refer to it as `JetAcc` (A. Tramacere 2021, in preparation).

4.1.3. Radio Jet

To model the radio jet emission, we have used the `JetSeT` multizone radio jet model `RadioJet`. This model implements a continuous jet as a sum of N_c single zones, following the approach of Kaiser (2006), where for each zone the values of R and B are ruled by Equation (3), and the particle density scales as

$$N_{s,i} = N_{s,0}(z_{s,0}/z_i)^{m_N}, \quad (2)$$

where $N_{s,0}$ is the initial density of emitters at the starting point of the radio jet $z_{s,0}$, z_i is the average position of the $i_{\rm th}$ component, and m_N is the index of the particle density law fixed to 2. The initial particle density is a fraction $N_{\rm frac}$ of that present in the acceleration region, and we fix it to 1. The radio jet extends from $z_{\rm radio}^{\rm start} = (z_{\rm acc} + R_{\rm acc})K_R^{\rm start}$ to $z_{\rm radio}^{\rm end}(z_{\rm acc} + R_{\rm acc})K_R^{\rm end}$, where $K_R^{\rm start}$ and $K_R^{\rm end}$ are free parameters. In the present analysis we fix $K_R^{\rm start} = 1$, and $K_R^{\rm end}$ is fixed in order to match the value of 1×10^{15} cm according to the analysis presented in Bright et al. (2020). The particle distribution in each region has the same spectral law as in the acceleration region, but we decrease the value of $\gamma_{\rm cut}$ to take into account the effect of the cooling when the particles leave the acceleration region. In our analysis we take into account only synchrotron cooling, and we evolve $\gamma_{\rm cut}$ according to Equation (27) in Kaiser (2006). More details about the connection between the acceleration and radio are discussed in Section 4.3.

4.2. Phenomenological Model Setup

As a first step we set the geometrical properties of the jet, i.e., we define the extent of the preacceleration, acceleration, and radio emission sites, and the values of the magnetic field. We assume that the jet is launched at distance z_0 from the BH, with an initial cross section R_0, and that the bulk Lorentz factor ($\Gamma_{\rm jet}$) of the jet is constant over the full jet extent. The acceleration region starts at a distance $z_{\rm acc}^{\rm start}$ with a width equal to jet cross section diameter $R_{\rm acc} = 2R(z_{\rm acc})$, and we treat it as a spherical region. The radio region starts at $z_{\rm radio}^{\rm start} = K_R^{\rm start}(z_{\rm acc} + R_{\rm acc})$ and ends at a distance $z_{\rm radio}^{\rm end} = K_R^{\rm end}(z_{\rm acc} + R_{\rm acc})$ (a scheme of the model is presented in Figure 6). According to Bright et al.

(2020), we fix the distance of the jet from the observer to the value of $d = 3$ kpc, the termination of the radio jet to the value of $z_{\rm end} \approx 1 \times 10^{15}$ cm, and the value of the beaming factor to $\delta = [\Gamma_{\rm jet}(1 - \beta_{\rm jet}\cos(\theta_{\rm obs})]^{-1} \approx 2.2$, using the values of $\beta_{\rm jet} = 0.89$ and $\theta_{\rm obs} = 63°$ reported in Bright et al. (2020). We assume a ballistic jet model (Begelman et al. 1984; Kaiser 2006) characterized by

$$\begin{aligned} B(z) &\propto B_0(z_0/z)^{m_B} \\ R(z) &\propto R_0(z/z_0)^{m_R} \\ N(z) &\propto R_0(z_0/z)^{m_N}, \end{aligned} \tag{3}$$

with $m_B \approx 1$, $m_R = 1$, and $m_N = 2.0$. This choice assumes that the jet is very close to the ballistic regime, with a magnetic field dominated by the toroidal component, and justifies the assumption that the bulk Lorentz factor is constant along the jet.

We use a BH mass of $M_{\rm BH} = 8M_\odot$. The jet luminosity $L_{\rm jet}$ is linked to the Eddington luminosity ($L_{\rm Edd}$) according to

$$L_{\rm jet} = \frac{1}{2} q_{\rm jet} L_{\rm Edd}, \tag{4}$$

where $L_{\rm Edd} \approx 1.3 \times 10^{38}(M_{\rm BH}/M_\odot)$ erg s^{-1} (Rybicki & Lightman 1986). It is worth noting that our $q_{\rm jet}$ parameter is not linked directly to the accretion efficiency process, because the jet powering could, in principle, be supported also by other mechanisms such as the Blandford–Znajek mechanism (Blandford & Znajek 1977), which predicts electromagnetic extraction of energy and angular momentum from the magnetized accretion disk surrounding a BH. Hence, our $q_{\rm jet}$ parameter should not be used to infer or constrain the accretion efficiency, and it will be discussed in a more accurate physical context in A. Tramacere (2021, in preparation).

We assume that the jet is launched at a distance $z = z_0$ from the BH with $z_0 = 50R_S \approx 1.2 \times 10^8$ cm, where $R_S = (2GM_{\rm BH})/c^2$. The launching jet position $z = z_0$ in the current analysis is assumed constant, to reduce the model complexity, and it is chosen according to reference values published in a previous analysis (Vila & Romero 2010). The initial radius of the jet is set to $R(z_0) = 0.1z_0$, resulting in an opening angle of $\theta_{\rm open} \approx 5.^\circ 7$. We impose that in the launching region the entire jet power is in the form of magnetic energy

$$L_{\rm jet} = L_B(z_0) = \pi U_B(z_0) R(z_0)^2 \Gamma_{\rm jet}^2 \beta_{\rm jet} c, \tag{5}$$

where $U_B = B^2/(8\pi)$, and setting $q_{\rm jet} = 0.2$, we obtain $B_0 \approx 6.8 \times 10^6$ G.

The value of m_B can be constrained from the spectral index of radio jet emission, $\alpha_R \approx 0.15$, according to Equation (39) in Kaiser (2006), which refers to the case of strong radiative cooling and almost constant value of the electron distribution high-energy cutoff. According to this scenario, which is very similar to what we expect in our case, we can rearrange Equation (39) in Kaiser (2006) as

$$m_B = \frac{1 + m_R}{2 - \alpha_R}, \tag{6}$$

which is similar to the trend of the thick radio spectrum discussed in Pe'er & Casella (2009), and we obtain a value of $m_B \approx 1.1$. We stress that this is an initial guess done assuming that the jet is not changing after the acceleration region. As we will discuss in the next section, during the model fit we need to take into account that jet expansion might change above the acceleration region; hence, we will relax the constraint on m_B and m_R considered in the `RadioJet` emission.

To constrain the value of $z_{\rm acc}$, we impose that $R_{\rm acc} = R(z_{\rm acc})$, $B_{\rm acc} = B(z_{\rm acc})$, and $N_{e,\rm acc}$ correspond to a synchrotron self-absorption frequency of $\nu_t \approx 1.5 \times 10^{13}$ Hz. This value of ν_t is obtained from the phenomenological fit of the optically thin to optically thick synchrotron emission between millimeter and optical data shown in Figure 2. In order to solve this problem, we combine the analytical expression of the synchrotron self-absorption frequency (ν_t; Rybicki & Lightman 1986), evaluated at the peak (i.e., $\alpha_\nu = 0$),

$$\nu_t = \nu_L \left[\frac{\pi\sqrt{\pi}}{4} \frac{qR_{\rm acc}N_{e,\rm acc}}{B_{\rm acc}} f_k(s) \right]^{\frac{2}{s+4}}, \tag{7}$$

and that of the synchrotron emissivity (Rybicki & Lightman 1986) $\epsilon_s(\nu)$,

$$\epsilon_s(\nu) = \frac{F_\nu d_L^2}{V} = \frac{3\sigma_T c N_{e,\rm acc} U_B^{\rm acc}}{16\pi\sqrt{(}\pi)\nu_L} f_\epsilon(s), \tag{8}$$

where q is the electron charge, $U_B^{\rm acc}$ is the value of the magnetic field, V is the volume of a spherical geometry of volume V of radius $R_{\rm acc}$, s is the slope of the electron distribution power law, and $\nu_L = \frac{qB}{2\pi m_e c}$ is the Larmor frequency, and where the functions $f_k(s)$ and $f_\epsilon(s)$ are approximated to percent accuracy as reported in Ghisellini (2013). The value of s is obtained using the optically thin spectral index $\approx$0.6 from the phenomenological fit in Figure 2, according to the relation $s = 2\alpha + 1 \approx 2.2$ (Rybicki & Lightman 1986). We solve Equation (8) with respect to $N_e^{\rm acc}$ and then substitute in Equation (7), and we insert the functional form of $B = B(z_{\rm acc})$ and $R = R(z_{\rm acc})$ according to Equation (3). The final equation solved with respect to $z_{\rm acc}$ reads

$$z_{\rm acc} = \left[\left(\frac{\nu_t 2\pi m_e c}{qB_0^2 z_0^{m_B}} \right)^{\frac{s+4}{2}} \frac{3\sigma_T (B_0R_0)^2 f_\epsilon(s) z_0^{2\Delta_m}}{16 r_e^2 \pi^3 f_k(s) F_\nu d_L^2} \right]^{\psi}, \tag{9}$$

where $r_e = q^2/(m_e c^2)$ is the classical electron radius, $\Delta_m = m_B - m_R$, and $\psi = \frac{2}{4\Delta_m - m_B(s+4)}$.

Consequently, the starting position of the radio jet is set to $z_{\rm radio}^{\rm start} = z_{\rm acc}^{\rm end} = z_{\rm acc} + R_{\rm acc} \approx 3.1 \times 10^{10}$ cm, with an extent derived from Bright et al. (2020) of $z_{\rm end} \gtrsim 30000 z_{\rm radio}^{\rm start}$.

The value of the cutoff of the electron distribution is set to $\gamma_{\rm cut} = 60$, in order to produce the peak of the synchrotron emission above the IR frequencies for a magnetic field $B_{\rm acc} \approx 1.8 \times 10^4$ G, with a power-law slope $s \approx 2.1$ that is slightly lower than the value derived from the optically thin spectral index.

The constrained value of $z_{\rm acc}$ can be used to derive the hadronic content of the jet energetic in the form of cold protons. Following Vila & Romero (2010), we impose that in the acceleration region of the jet the magnetic energy of the jet is in subequipartition with the bulk kinetic energy of the cold protons, a condition that is mandatory to allow the mechanical compressibility of the plasma (Komissarov et al. 2007). We define the parameter $\rho_{p,B}^{\rm acc} = U_p(z_{\rm acc})/U_B(z_{\rm acc})$, where $U_p(z) = n_p(z)m_p c^2$, and we require that $\rho_{p,B} > 1$. This choice sets a value of cold proton luminosity in the acceleration region $L_p(z_{\rm acc}) > 3.6 \times 10^{37}$ erg s^{-1}. The input and output parameters for the phenomenological setup are listed in Table 4.

Table 4
Phenomenological Setup Parameters

Input Parameters		
Par. Name	Units	Input Value
z_0	cm	1.12×10^8
r_0	cm	1.12×10^7
$M_{\rm BH}$	$M_\odot$	8
$q_{\rm jet}$		0.20
F_ν^t	Jy	0.5
ν_t	Hz	1.5×10^{13}
s		2.1
$\rho_{p,B}^{\rm acc}$		>1
m_B		1.1
m_R		1.0
Output Parameters		
Par. Name	Units	Output Value
B_0	G	6.8×10^6
$B_{\rm acc}$	G	1.8×10^4
$L_p^{\rm acc}$	erg s^{-1}	$>3.6 \times 10^{37}$
$z_{\rm acc}^{\rm start}$	cm	2.4×10^{10}
$z_{\rm acc}^{\rm end}$	cm	2.9×10^{10}
$z_{\rm acc}$	cm	2.6×10^{10}
$R_{\rm acc}$	cm	2.6×10^9
$z_{\rm radio}^{\rm start}$	cm	2.9×10^{10}
$z_{\rm radio}^{\rm end}$	cm	$\gtrsim 1 \times 10^{15}$

4.3. Model Fit and Results

4.3.1. Initial Model Setup

To optimize the model, we use the composite model interface `FitModel` provided by `JetSeT`, which allows combining different models in a global model. This model can be optimized by inserting it into the `ModelMinimizer` `JetSeT` plug-in. In the current analysis we use a frequentist approach, and we use the `Minuit ModelMinimizer` option. We have used the `Data` and `ObsData` `JetSeT` tools to import the observed data, and we have added a 5% systematic error in the range $[1 \times 10^8, 1 \times 10^{16}]$ Hz, to avoid that the large inhomogeneity on the fractional error between radio and optical/UV data could bias the fit convergence. For the error estimate we provide only errors derived from the `MIGRAD` module of `Minuit`; a more reliable estimate based on a Markov Chain Monte Carlo (MCMC) will be presented in A. Tramacere (2021, in preparation).

The `DiskIrrComp` model, the `Comp. hump` model, and the `JetAcc` are independent; on the contrary, `JetAcc` and `RadioJet` are bound.

The initial values of the parameters for the `DiskIrrComp` model are chosen according to the analysis presented in Sections 3.3 and 3.4. In detail, we set the initial values of $L_{\rm disk} = 1 \times 10^{37}$ erg s^{-1}, $r_{\rm out} = 5000$, $f_{\rm out} = 0.01$, and $L_{\rm Comp}^{\rm ratio} = 4.5$, and we fix the inner disk temperature to $T_{\rm Disk} = 1.55 \times 10^6$ K, along with parameters $r_{\rm irr} = 1.1$ and $f_{\rm in} = 0.1$, the choice adopted in Gierliński et al. (2009), when the Comptonization of the outer disk is included in the irradiated disk.

For the `JetAcc` model, we fix $\theta_{\rm jet} = 63°$ and $\Gamma_{\rm jet} = 2.19$; we put a relative bound of ±0.5 centered on the parameter values derived in the previous section, $R_{\rm acc} = 2.6 \times 10^{19}$ cm and $B_{\rm acc} \approx 1.8 \times 10^4$ G; we freeze the initial value of $z_{\rm acc} = 2.6 \times 10^{10}$ cm; and we leave free the parameters for the electron distribution.

The initial setup of the parameters of the `RadioJet` is more complex, and we need to take into account the physical connection with the acceleration region and the cooling process. This effect plays a crucial role; indeed, as already discussed in Kaiser (2006) and Pe'er & Casella (2009), the combination of synchrotron cooling and jet expansion (assuming a negligible contribution from adiabatic cooling) will result in an asymptotic value of $\gamma_{\rm cut}(t)$, which can naturally explain the flat radio spectrum without the need to introduce significant particle re-acceleration in the radio jet. We follow the approach reported in Pe'er & Casella (2009; in the case of negligible adiabatic cooling), and we set $m_B^{\rm radio} = m_R^{\rm radio} = m_{\rm jet}$. The particle cutoff evolution in the radio jet will evolve according to Kaiser (2006):

$$\gamma_{\rm cut}(t) = \frac{\gamma_{\rm cut}}{1 + \frac{\sigma_T B 0^2}{6 m_e c \pi (f)} \gamma_{\rm cut} t_0^{1-f} (t^f - t_{\rm inj}^f)}, \quad (10)$$

where $f = 1 - 2m_{\rm jet}$ and $t_0 = z_0/\beta_{\rm jet} c \Gamma_{\rm jet}$, $t_{\rm inj} = z_{\rm inj}/\beta_{\rm jet} c \Gamma_{\rm jet}$, and $t = z_{//}/\beta_{\rm jet} c \Gamma_{\rm jet}$ are the comoving timescales. We freeze a starting value of $z_{\rm inj} = z_{\rm acc}^{\rm start} \approx 2.5 \times 10^{10}$ cm.

Another effect to take into account is the fact that for $z > z_{\rm acc}$ the structure of the jet could change; for this reason we leave free the parameter $m_{\rm jet}$ with a fit boundary of [0.5, 1.5], with an initial value of 1.18, which is slightly larger than the value used for the phenomenological constraining but gives a better agreement with radio to optical data.

The density of emitters at the base of the `RadioJet` is bound to be equal to the density of emitters in the acceleration region N_e calculated according to Equation (3), at $z = z_{\rm radio}^{\rm start}$, by fixing $N_{\rm frac} = 1.0$. We fix the values of $K_R^{\rm end} = 3000$ and $K_R^{\rm start} = 1$.

A list of the free and frozen parameters and of the bounds is given in Table 5 in the columns "Starting values" and "Fit boundaries," respectively.

4.3.2. Model Fit Results for the Disk and Corona Emission

We fit first the `DiskIrrComp` and `Comp. hump` components restricting the fit range to $\nu = [5 \times 10^{14}, 10^{20}]$ Hz, and we get $\chi^2 = 152$ for 98 degrees of freedom ($N_{\rm dof}$), corresponding to reduced $\chi^2_{\rm red} = 1.55$. The parameters values are reported in the upper part of Table 5.

The best-fit parameters resulting from `JetSeT` are similar to those obtained from the `XSPEC` analysis for the `diskir` model, in particular, the $r_{\rm out}$ value ($3.58 \times 10^3 R_{\rm in}$ and $3.45 \times 10^3 R_{\rm in}$) and L_C/L_D (4.1 and 4.6) for `JetSeT` and `XSPEC`, respectively. The $f_{\rm out}$ parameter is unconstrained for both `XSPEC` and `JetSeT`. However, a well-constrained value is obtained when the jet component is added as shown in Section 4.3.3. Because the `JetSeT` model for the Comptonized emission is phenomenological, the high-energy range of the irradiated disk is fit as a cutoff power law and thus is not directly comparable to the `diskir` parameters. For that portion of the spectrum, `JetSeT` found $\Gamma = 1.64$ (compared to 1.78 from `diskir`) and $E_C = 150$ keV (compared to $kT_e = 58$ keV from `diskir`). We do note that $E_C/kT_e \approx 2.6$, which falls within the predicted range of ratios between cutoff energy and electron temperature (Petrucci et al. 2000, 2001), suggesting that the values are in agreement, even though the incertitude on the `JetSeT` value is quite large.

Table 5
JetSeT Best-fit Model Parameters

Model Name	Par. Name	Units	Best-fit Value	Error	Starting Values	Fit Boundaries	Frozen
CompHump	$E_{\rm hump}$	keV	26	14	20	[15; 35]	False
"	$\Gamma_{\rm hump}$		−0.5	2	−1.2	[−2; 2]	False
DiskIrrComp	$T_{\rm Disk}$	K			1.55×10^{6}		True
"	$L_{\rm Disk}$	erg s^{-1}	1.09×10^{37}	1.0×10^{32}	1×10^{37}	$[1 \times 10^{36}; 1 \times 10^{39}]$	False
"	$r_{\rm out}$		3.58×10^{3}	0.21×10^{3}	5×10^{3}	[1; -]	False
"	$r_{\rm irr}$				1.1		True
"	$\Gamma_{\rm Comp}$		1.64	0.12	1.65	[1.3; 1.9]	False
"	$E_{\rm Comp}$	keV	150	100	140	[20; 200]	False
"	$L_{\rm Comp}^{\rm ratio}$		4.1	0.6	4.5	[0; -]	False
"	$f_{\rm in}$				0.1		True
"	$f_{\rm out}$		1×10^{-2}	40×10^{-2}	0.01	[0; -]	False
DiskIrrComp	$r_{\rm out}$		3.4×10^{3}	0.5×10^{3}	3.58×10^{3}	[1; -]	False
"	$f_{\rm out}$		7.33×10^{-3}	0.15×10^{-3}	1×10^{-2}	[0; -]	False
"	$L_{\rm Comp}^{\rm ratio}$		4.270	0.016	4.1	[0; -]	False
JetAcc	$N_{e,\rm acc}$	cm^{-3}	9.998×10^{11}	0.001×10^{11}	1.0×10^{12}	[0; -]	False
"	s		2.082	0.007	2.1	[-; -]	False
"	$\gamma_{\rm cut}$		65.4	1.7	60	[1; -]	False
"	$R_{\rm acc}$	cm	2.6×10^{9}	1.0×10^{1}	2.6×10^{9}	$[1.32 \times 10^{9}; 3.96 \times 10^{9}]$	False
"	$z_{\rm acc}$	cm			2.8×10^{10}		True
"	$B_{\rm acc}$	G	17986	1.0×10^{-3}	17986	[8993; 26980]	False
"	$\theta_{\rm jet}$	deg			63		True
"	$\Gamma_{\rm jet}$				2.19		True
RadioJet	$z_{\rm inj}$				2.5×10^{10}		True
"	$N_{\rm frac}$				1		True
"	$K_R^{\rm start}$				1		True
"	$K_R^{\rm end}$				30000		True
"	$m_{\rm jet}$		1.203	0.001	1.1	[0.5; 1.5]	False

4.3.3. Model Fit Results for the Jet Emission

To fit the full-band SED, we freeze all the parameters in the CompHump and DiskIrrComp components, except for $r_{\rm out}$, $f_{\rm out}$, and L_C/L_D, and we fit the global model over the full SED band in the range $\nu = [5 \times 10^{8}, 10^{20}]$ Hz.

The model fit converged with a final $\chi^2 = 181$ for 122 degrees of freedom ($N_{\rm dof}$), corresponding to a $\chi^2_{\rm red} = 1.48$. The parameter values are reported in the bottom part of Table 5, and the parameters derived from the best-fit model are reported in Table 6 with the SED model plotted in Figure 7. Regarding the DiskIrrComp, we note that adding the jet component results in a better constraint on the value of $f_{\rm out} = (7.33 \pm 0.15) \times 10^{-3}$, which is in the expected range of other BH binaries in the hard state (Gierliński et al. 2009). Moreover, restricting the fit statistics to the same interval used in the XSPEC analysis, we get a $\chi^2 = 157$ with $N_{\rm dof} = 107$, corresponding to a $\chi^2_{\rm red} = 1.6$. Regarding the jet component, we note that final best-fit model parameters did not change significantly from the input values, suggesting that the phenomenological setup was able to find a configuration very close to the optimal one, even though the fit might be biased by the degeneracy among some parameters. We will investigate this problem in a forthcoming work (A. Tramacere 2021, in preparation), by means of a Bayesian approach based on the MCMC technique. In general, we find that our assumption based on the connection between a compact acceleration region feeding the extended radio jet is able to model self-consistently the UV to optical emission, reproducing the observed flat radio spectrum. In particular, we find that, according to our best-fit model, the particles in the radio region reach the asymptotic value of $\gamma_{\rm cut} \approx 8$ and keep it almost constant as result of the decrease in the cooling synchrotron cooling rate due to the jet expansion. This behavior is in agreement with the results of Pe'er & Casella (2009) and Kaiser (2006) for the case of synchrotron cooling dominating over the adiabatic one. It is worth discussing some specific parameters in detail:

Table 6
Model Parameters Evaluated from the Best-fit Model

Par. Name	Units	Value	Setup Value
$q_{\rm jet}$		>0.15	0.20
U_e/U_B		0.18	⋯
$N_e^{\rm acc}/N_p^{\rm cold}$		<94	⋯
$L_{\rm jet}^{\rm acc}$	erg s^{-1}	$>8.0 \times 10^{37}$	⋯
$L_{\rm rad}^{\rm acc}$	erg s^{-1}	1.1×10^{36}	⋯
$L_B^{\rm acc}$	erg s^{-1}	3.6×10^{37}	3.6×10^{37}
$L_e^{\rm acc}$	erg s^{-1}	6.6×10^{36}	⋯
$L_p^{\rm acc}$	erg s^{-1}	$>3.6 \times 10^{37}$	$>3.6 \times 10^{37}$

1. $q_{\rm jet} > 0.15$. This value is compatible with the input value $q_{\rm jet} = 0.2$. As already discussed in the previous section, the $q_{\rm jet}$ parameter is not linked directly to the accretion efficiency because the jet powering could, in principle, be supported also by other mechanisms such as the Blandford–Znajek mechanism (Blandford & Znajek 1977), which takes into account advection of magnetic flux from an accretion disk surrounding the BH. Hence, our $q_{\rm jet}$ parameter cannot be used to infer or constrain the accretion efficiency.
2. $U_e/U_B = 0.18$. The U_e/U_B is not far from equipartition, and it is obtained without providing any constraint. This proves that the combination of the phenomenological

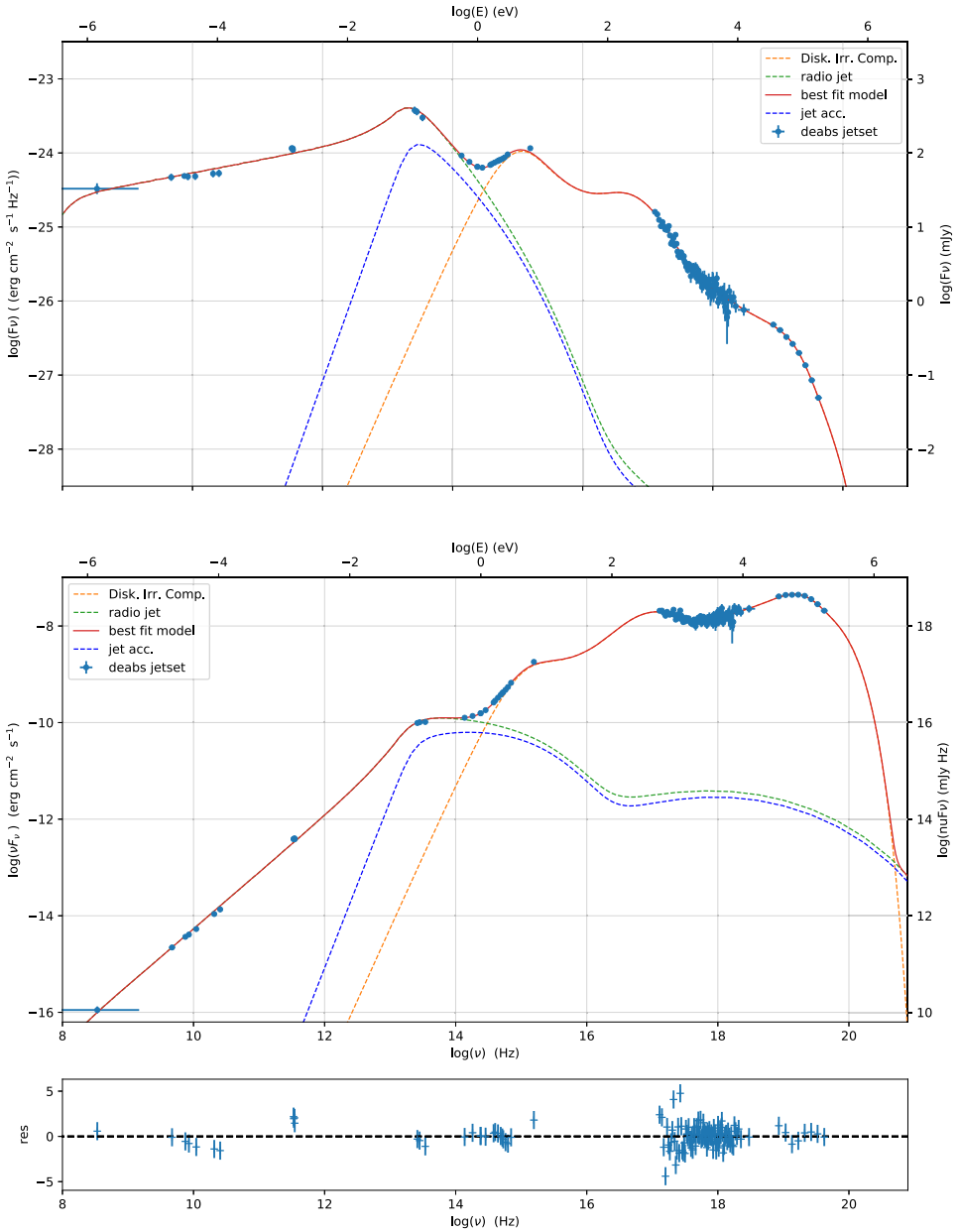

Figure 7. Best-fit `JetSeT` model of the broadband SED. Top panel: F_ν representation of the global model fit. Bottom panel: νF_ν representation. The red line represents the global model, the dashed lines correspond to the single components, and the color is reported in the legend. The best-fit parameters are reported in Table 5. The residuals plot is evaluated with respect to the νF_ν representation.

model setup and the minimization of the global model converged naturally toward a configuration close to the physical equipartition of U_e and U_B, giving further support to the choice of a compact acceleration region that is connecting the preacceleration region to the radio jet.

3. $N_e^{\rm acc}/N_p^{\rm cold} < 94$. Since our model is leptonic, the content of cold protons can be derived from ancillary conditions, as the condition that the magnetic energy of the jet has to be in subequipartition with the bulk kinetic energy of the cold protons, in order to allow the mechanical compressibility of the plasma (Komissarov et al. 2007), and formation of shocks/turbulent acceleration sites in the acceleration region. From the best-fit model we get that to respect the condition $\rho_{p,B}^{\rm acc} > 1.0$ we need to impose a lower limit of the ratio of relativistic electrons to cold protons $N_e/N_p^{\rm cold} < 112$. This value is compatible with the usual value of $N_e/N_p^{\rm cold} = 10$ (Celotti & Ghisellini 2008) used in the case of relativistic jets with a leptonic radiative domination. Moreover, we note that the value of $B_{\rm acc}$ obtained from the best fit did not require a significant change in the value of L_B as derived from the phenomenological model setup, demonstrating that constraining $z_{\rm acc}$ based on the value of ν_t is naturally in agreement with formation of mechanical compression in the jet when $U_p > U_B$.
4. $m_{\rm jet} = 1.2$. The value of $m_{\rm jet}$ is one of the most critical; indeed, it dictates the topology and intensity of the magnetic field beyond the acceleration region, and it is interesting to compare to the value of m_B that is used to

model the jet below the acceleration region. The initial guess based on the value of α_R has required a small modification in order to reproduce the observed radio spectrum, and the final model naturally explains the almost flat radio spectrum as emission of the cooled electron leaving the acceleration region.

5. Discussion and Conclusions

As MAXI J1820+070 was observed numerous times across the EM spectrum during its outburst, there are multiple works relevant to portions of our multiwavelength analysis, though to date none study the source in such a complete picture as is presented with our model from `JetSeT`.

Shidatsu et al. (2018) provide the most direct comparison to the analysis in this work, though the source behavior is different before and after March 26 (MJD 58206). They found that the optical and NIR emission is not entirely from disk emission and thus included a power law to their `diskir` model with a spectrum described by fixed parameters $kT_{\rm disk} = 0.35$ keV, $L_C/L_D = 70$, $f_{\rm out} = 5 \times 10^{-3}$, and $R_{\rm out} = 10^5 R_{\rm in}$. Our fit found a considerably lower $kT_{\rm disk}$ (0.12 keV), L_C/L_D (4.7), and $R_{\rm out}$ ($10^3 R_{\rm in}$) but a higher $f_{\rm out}$ (4×10^{-2}). We note that the source behavior between the two observations is different with changes in the spectral hardness in hard X-rays (Roques & Jourdain 2019), the development of type C QPOs (Stiele & Kong 2020), and a reduction in the size of the corona (Kara et al. 2019) that can possibly explain the differences.

Following the work of Muñoz-Darias et al. (2019), we explored the presence of disk wind signatures in our VLT/X-shooter optical spectrum, as this data set falls between epochs 11 and 12 of the Muñoz-Darias et al. (2019) campaign and adds an epoch in their uncovered time window (between March 26 and April 23). We focus our spectral analysis on the He I λ5876, He I λ6678, and Hα wavelength regions. We found shallow P Cygni profiles and strong line asymmetries in all three mentioned lines, while a broad outflow component is detected only in the red wing of the Hα. Among the observed absorption troughs, the one detected in the blue wing of He I λ5876 is the more prominent, and it results in a terminal wind velocity $v_t = 880\,{\rm km\,s^{-1}}$, which is consistent with the outflow velocity of $v \sim 900\,{\rm km\,s^{-1}}$, derived from the H$\alpha$ redshifted broad component. These properties indicate that at this epoch optical disk winds are still present, although with slower velocities with respect to what was found in Muñoz-Darias et al. (2019). The authors also report an evolution of the line profiles during their monitoring campaign, and our observation confirms this trend. In particular, the observed Hα profile can be interpreted as a continuation in the evolving pattern of the line between epochs 9 and 12 shown in Figure 2 of Muñoz-Darias et al. (2019). Similar spectral variations were previously reported by Tucker et al. (2018) and ascribed to the orbital motion of the system. Interestingly, some of the most conspicuous optical wind detections in Muñoz-Darias et al. (2019) occur in epochs corresponding to the hard state of the source, when radio emission and strong jet activity are present (Bright et al. 2020) and the peak of the optical outburst of the source is reported. This led the authors to the conclusion that the optical wind detected in MAXI J1820+070 is simultaneous with the jet. Our wind signature detection, together with the results from our broadband spectral analysis, is consistent with this scenario.

Our phenomenological analysis of the compact jet found that the data could be modeled by a broken power law with $\alpha_{\rm thick} = 0.28 \pm 0.02$ and $\alpha_{\rm thin} = -0.61 \pm 0.01$. Combining observations from late March and early April, Russell et al. (2018) performed a similar analysis and found spectral indices of $\alpha_{\rm thick} \sim 0.3$ and $\alpha_{\rm thin} \sim -0.7$. Building on Russell et al. (2018), Shidatsu et al. (2018) estimated a transition frequency of $\sim 3 \times 10^{13}$ Hz and a corresponding flux density of $\sim$0.4 Jy. From these values they determined $B \sim 1 \times 10^4$ G and $R \sim 2 \times 10^9$ cm using equations from Shidatsu et al. (2011). Our model peaks at $(1.6 \pm 0.2) \times 10^{13}$ Hz with a flux density of $\sim$0.35 Jy, thus resulting in similar values.

These values are in agreement with the phenomenological setup and with the best-fit model from `JetSeT`. In particular, the `JetSeT` best-fit model gives a magnetic field in the acceleration region of $\approx 1.8 \times 10^4$ G and a region radius of $\approx 2.6 \times 10^9$ cm.

The corresponding energy density of the magnetic field is $\approx 1.3 \times 10^7\,{\rm erg\,cm^{-3}}$, compared to the value of $8 \times 10^6\,{\rm erg\,cm^3}$ from Shidatsu et al. (2018).

Additionally, we identify separate radio spectral components at frequencies below $\sim$10 GHz, showing an inverted power-law spectrum with slope $\alpha = 0.11 \pm 0.02$. Bright et al. (2020), collecting data from different epochs of VLA, Multi-Element Radio Linked Interferometer Network (eMERLIN), and Meer Karoo Array Telescope (MeerKAT) observations, could identify at least one ejected component during the transition from the hard to the soft state (2018 mid-June to mid-September). Though the source is unresolved down to a subarcsecond resolution in the VLA observations considered here (collected in a previous epoch), the presence of an additional low-frequency spectral component could suggest that the ejecta later detected by Bright et al. (2020) were already present at a subparsec scale during the 2018 April 12 epoch considered here.

This component is represented in the `JetSeT` broadband model by the `RadioJet` component and stems naturally from the cooling of the accelerated particle leaving the acceleration region. Interestingly, we find that the best-fit index $m_{\rm jet} \approx 1.2$ predicts a radio spectral index of $\alpha = 1 - 1/m_{\rm jet} \approx 0.166$ that is close to the value found in the power-law fit. We note that the small difference between the two values is due to the fact that the `JetSeT RadioJet` model takes into account the data range from radio to millimeter frequencies, differently from the power-law fit, whose range extends up $\approx 10^{10}$ Hz.

In conclusion, our broadband analyses of MAXI J1820+070 found the source in a hard state with parameters similar to what was reported by Shidatsu et al. (2018) The `JetSeT` broadband model was able to reproduce the full SED taking into account both the disk/corona emission and the leptonic radiatively dominated relativistic jet contribution. We found that the relativistic jet required a total energy of $L_{\rm jet} \geqslant 8.0 \times 10^{37}\,{\rm erg\,s^{-1}}$, corresponding to $0.15 L_{\rm Edd}$. This value represents a lower limit, since we assume that the hadronic content of the jets is only in terms of cold protons, without a significant radiative contribution. The flat radio spectral shape stems naturally from the synchroton cooling of the electrons in the acceleration regions, in agreement with previous analyses (Kaiser 2006; Pe'er & Casella 2009). In comparison, the accretion luminosity (6×10^{37} erg s^{-1}) is comparable to the lower limit of the jet luminosity. Thus, in MAXI J1820+070 it is possible for the jet to be powered predominately via accretion with only a small contribution from the Blanford–Znajek mechanism,

which in this case cannot provide much power since the BH spin is reported to be low (Buisson et al. 2019; Zhao et al. 2000).

We thank the Italian node of the European ALMA Regional Centre (ARC) for support. J.R. and G.B. acknowledge financial support under the INTEGRAL ASI-INAF agreement 2019-35-HH.0 and ASI/INAF No. 2017-14-H.0. F.O. acknowledges the support of the H2020 European Hemera program, grant agreement No. 730970. The research leading to these results has received funding from the European Union's Horizon 2020 Programme under the AHEAD2020 project (grant agreement No. 871158) F.O. acknowledges the support of the H2020 European Hemera program, grant agreement No. 730970, and the support of the GRAWITA/PRIN-MIUR project: "*The new frontier of the Multi-Messenger Astrophysics: follow-up of electromagnetic transient counterparts of gravitational wave sources*." Based on observations with INTEGRAL, an ESA project with instruments and science data center funded by ESA member states (especially the PI countries: Denmark, France, Germany, Italy, Switzerland, Spain) and with the participation of Russia and the USA. This research has made use of the services of the ESO Science Archive Facility. Based on observations collected at the European Southern Observatory under ESO programs 2017.1.01103.T (ALMA) and 0101.D-0356(A) (VLT). ALMA is a partnership of ESO (representing its member states), NSF (USA), and NINS (Japan), together with NRC (Canada) and NSC and ASIAA (Taiwan), in cooperation with the Republic of Chile. The Joint ALMA Observatory is operated by ESO, AUI/NRAO, and NAOJ. The National Radio Astronomy Observatory is a facility of the National Science Foundation operated under cooperative agreement by Associated Universities, Inc.

ORCID iDs

J. Rodi https://orcid.org/0000-0003-2126-5908
A. Tramacere https://orcid.org/0000-0002-8186-3793
F. Onori https://orcid.org/0000-0001-6286-1744
G. Bruni https://orcid.org/0000-0002-5182-6289
M. Fiocchi https://orcid.org/0000-0001-5697-6019

References

Astropy Collaboration, Robitaille, T. P., Tollerud, E. J., et al. 2013, A&A, 558, A33
Bassi, T., Malzac, J., Del Santo, M., et al. 2020, MNRAS, 494, 571
Begelman, M. C., Blandford, R. D., & Rees, M. J. 1984, RvMPh, 56, 255
Blandford, R. D., & Znajek, R. L. 1977, MNRAS, 179, 433
Bonato, M., Liuzzo, E., Giannetti, A., et al. 2018, MNRAS, 478, 1512
Bright, J. S., Fender, R. P., Motta, S. E., et al. 2020, NatAs, 4, 697
Buisson, D. J. K., Fabian, A. C., Barret, D., et al. 2019, MNRAS, 490, 1350
Cardelli, J. A., Clayton, G. C., & Mathis, J. S. 1989, ApJ, 345, 245
Celotti, A., & Ghisellini, G. 2008, MNRAS, 385, 283
Clarke, T. E., Kassim, N. E., Arisken, W., et al. 2016, Proc. SPIE, 9906, 99065B
Flewelling, H. A., Magnier, E. A., Chambers, K. C., et al. 2020, ApJS, 251, 7
Gallo, E., Fender, R. P., & Pooley, G. G. 2003, MNRAS, 344, 60
Ghisellini, G. 2013, Radiative Processes in High Energy Astrophysics, Vol. 873 (Berlin: Springer)
Gierliński, M., Done, C., & Page, K. 2009, MNRAS, 392, 1106
Kaiser, C. R. 2006, MNRAS, 367, 1083
Kara, E., Steiner, J. F., Fabian, A. C., et al. 2019, Natur, 565, 198
Kawamuro, T., Negoro, H., Yoneyama, T., et al. 2018, ATel, 11399, 1
Komissarov, S. S., Barkov, M. V., Vlahakis, N., & Königl, A. 2007, MNRAS, 380, 51
Merloni, A., Heinz, S., & di Matteo, T. 2003, MNRAS, 345, 1057
Mirabel, I. F., Rodriguez, L. F., Cordier, B., Paul, J., & Lebrun, F. 1992, Natur, 358, 215
Muñoz-Darias, T., Jiménez-Ibarra, F., Panizo-Espinar, G., et al. 2019, ApJL, 879, L4
Pe'er, A., & Casella, P. 2009, ApJ, 699, 1919
Petrucci, P. O., Haardt, F., Maraschi, L., et al. 2000, ApJ, 540, 131
Petrucci, P. O., Haardt, F., Maraschi, L., et al. 2001, ApJ, 556, 716
Polisensky, E., Giacintucci, S., Peters, W. M., Clarke, T. E., & Kassim, N. E. 2018, ATel, 11540, 1
Price-Whelan, A. M., Sipőcz, B. M., Günther, H. M., et al. 2018, AJ, 156, 123
Roques, J.-P., & Jourdain, E. 2019, ApJ, 870, 92
Russell, D. M., Baglio, M. C., Bright, J., et al. 2018, ATel, 11533, 1
Russell, D. M., Markoff, S., Casella, P., et al. 2013, MNRAS, 429, 815
Rybicki, G. B., & Lightman, A. P. 1986, Radiative Processes in Astrophysics (New York: Wiley)
Schlafly, E. F., & Finkbeiner, D. P. 2011, ApJ, 737, 103
Shappee, B. J., Prieto, J. L., Grupe, D., et al. 2014, ApJ, 788, 48
Shidatsu, M., Nakahira, S., Yamada, S., et al. 2018, ApJ, 868, 54
Shidatsu, M., Ueda, Y., Tazaki, F., et al. 2011, PASJ, 63, S785
Stiele, H., & Kong, A. K. H. 2020, ApJ, 889, 142
Tramacere, A. 2020, JetSeT: Numerical modeling and SED fitting tool for relativistic jets, Astrophysics Source Code Library, ascl:2009.001
Tramacere, A., Giommi, P., Perri, M., Verrecchia, F., & Tosti, G. 2009, A&A, 501, 879
Tramacere, A., Massaro, E., & Taylor, A. M. 2011, ApJ, 739, 66
Trushkin, S. A., Nizhelskij, N. A., Tsybulev, P. G., & Erkenov, A. 2018, ATel, 11539, 1
Tucker, M. A., Shappee, B. J., Holoien, T. W. S., et al. 2018, ApJL, 867, L9
Ubertini, P., Lebrun, F., Di Cocco, G., et al. 2003, A&A, 411, L131
Vernet, J., Dekker, H., D'Odorico, S., et al. 2011, A&A, 536, A105
Vila, G. S., & Romero, G. E. 2010, MNRAS, 403, 1457
Zdziarski, A. A., Malzac, J., & Bednarek, W. 2009, MNRAS, 394, L41
Zhao, X., Gou, L., Dong, Y., et al. 2020, arXiv:2012.05544